PERGAMON

International Journal of Heat and Mass Transfer 45 (2002) 5045–5051

International Journal of HEAT and MASS TRANSFER

www.elsevier.com/locate/ijhmt

Power laws for sizes and growth times of double-diffusive convection cells

Karsten Kötter, Mario Markus *

Max-Planck-Institut für molekulare Physiologie, Postfach 500247, 44202 Dortmund, Germany

Received 19 December 2001; received in revised form 3 May 2002

Abstract

We perform quantitative investigations of double-diffusive convection in a setup that is extremely easy to implement and to observe. In this setup, a drop (containing a surfactant, as destabilizing substance, and glycerine, as stabilizing substance, stirred in water) is injected at the bottom of a dish filled with water. After a few minutes, surfactant cells are formed. Later, fingers transporting surfactant grow upwards at the vertices of these cells. The size λ of the cells and their growth time T_{em} are observed with a light microscope; also, these quantities are estimated analytically and determined from PDE simulations. We obtain power laws for the dependence of λ and T_{em} on the initial concentration of the stabilizing substance; the exponents in these laws are widely independent of the experimental conditions and on the model assumptions.

Keywords: Convection; Double-diffusion; Fluids

1. Introduction

Transport by double-diffusive convection occurs in a wide variety of systems (see reviews in [1–3]). In the case of oceans, it is considered the most important mixing process because of the rapid transport of salt and heat (see [2]). The phenomenon occurs, for example in low and mid-latitude regions, as upper layers of water are heated by the sun and become richer in salt due to evaporation. Even if the upper layer is gravitationally stable, double-diffusive convection can cause salt transport downwards, which is explained as follows. A fluctuation consisting of a tongue-like intrusion of the upper layer (large temperature T and large salt concentration S) into the lower layer, will grow because it rapidly cools down, while it retains the gravitationally unstable S. (Note that the diffusivity of heat is much larger than that of salt.) The resulting "salt fingers" have also been observed on the Mediterranean outflow (larger S and T) over the Atlantic (lower S and T) [4]. In general, the formation of fingers is preceeded by the formation of cells (see [5]).

The same phenomenon, but involving components other than salt and temperature, has been seen to occur in the melt during the manufacture of alloys, causing undesired banded structures [3,6]. Also, in the magma below the earth's crust fingers have been detected as elongated intrusions or abrupt transitions after solidification [1,7]. In addition, magnetohydrodynamic calculations predict transport of angular momentum and "helium fingers" in stars [3,8,9]. Furthermore, this type of transport can cause the rising of polluting components from sewage mixtures, which are altogether heavier than water and are thus assumed to be safely disposed by a pipe on the bottom of the sea [1,10].

In the laboratory, this phenomenon has been studied so far in specially designed tanks with horizontal layers of solutions. These solutions have different compositions of salt and sugar, or salt and heat (see e.g. [1,2,11–14]). A typical experimental tank is sketched in Ref. [15]. In general, the traditional setups require several technical

* Corresponding author. Address: Max-Planck-Institut für molekulare Physiologie, Otto-Hahn-Strasse 11, 44227 Dortmund, Germany. Tel./fax: +49-231-133-2470/2699.

E-mail address: markus@mpi-dortmund.mpg.de (M. Markus).

0017-9310/02/$ - see front matter
PII: S0017-9310(02)00212-0

Nomenclature

A	perturbation of the interface
α_S, α_T	difference between density (of S and T) and ρ_0, relative to ρ_0
γ_T, γ_λ	exponents of power laws
D_S, D_T	diffusion coefficients of S and T
Δt	time step for numerical integration
$\vec{\epsilon}$	initial noise of fluid velocity
h	height of lower layer
λ	mean cell size (wavelength)
$\tilde{\lambda}$, $\tilde{T}_{\mathrm{em}}$	values of λ and T_{em} for $T_0 = 2.5\%$
Λ	growth rate of perturbations
ν	kinematic viscosity
p	pressure
ρ_0	density of water
R_ρ	stability ratio
r_ρ	T_0/S_0
ρ_S, ρ_T	densities of S and T
S	destabilizing component (e.g. salt or surfactant) and its concentration
S_0, T_0	initial concentrations of S and T
$\overline{S}_z$, $\overline{T}_z$	vertically averaged S_z and T_z
S_z, T_z	derivatives of the concentrations of S and T with respect to z
T	stabilizing component (e.g. temperature or glycerine) and its concentration
T_{em}	growth time (time at which absorption at minima of S is within 5% of absorption of a void dish)
$\vec{v}$	fluid velocity

considerations: (i) care has to be taken to obtain an accurate horizontal layering; (ii) for visualization, a dye (see e.g. [1,14,15]), which must not interact with the other substances, must be added; alternatively, a special optical equipment, e.g. to measure the refractive index [5,11–13], has to be implemented; (iii) distortion of the system through invasive techniques, such as withdrawing samples or inserting a conductivity probe or a thermocouple [12–15], must be minimized. As a result of these constraints, only a low number of often strongly scattering data points are obtained (see e.g. [12–15]). Furthermore, scaling laws of observables vs. control parameters have often been performed only for parameters changing by relatively small factors; (examples: size of fingers vs. the temperature gradient, the latter varying by a factor 5 [14], ratio of fluxes vs. the initial concentration of S, the latter varying by a factor 6 [12]).

In the present work we used the setup reported recently [16,17], which allows to perform fast and readily visible measurements, allowing to collect large amounts of data over wide parameter ranges, and which avoids the constraints (i)–(iii) listed above. In this setup, a drop is injected at the bottom of a dish with water. The drop contains: (a) glycerine, as fastly diffusing and therefore stabilizing substance T (higher density than water); (ii) a surfactant as slowly diffusing, destabilizing substance S (lower density than water); and (c) water. The surfactant forms large micelles (length: 4000 Å; [16]) that strongly scatter light and are thus clearly detectable by the bare eye or by a video camera. Furthermore, the low diffusivity of these micelles causes long-lasting optical definition of the observed structures (see [16,17]).

The region in which cells are formed is so thin in our setup (0.2 mm) that measurements can easily be performed by observing vertically through this region. A drawback of this method is that one can only measure averages and not spatial dependences in the vertical direction. Moreover, this setup is not suitable to determine vertical transport fluxes, which have been studied in most works so far (e.g. in [12–15,18]); therefore, we concentrate on the determination of the size and growth time of the cells.

2. Experiments

We mixed glycerine (density $\rho_T = 1.26$ g/cm^3), water, and the nonionic surfactant CH_3–$(CH_2)_3$–O–[CH_2–CH_2–O]$_{12}$–H (alcohol ethoxylate; density $\rho_S = 0.95$ g/cm^3). The initial concentration T_0 of glycerine in the mixture was varied, while holding the ratio $r_\rho = T_0/S_0$ constant (S_0 = initial concentration of the surfactant). The total density of the mixture was always larger than that of water. The mixture was stirred for 1–2 min and then 50 μl were injected (during 20 s) with a motorized pump at a constant rate at the center of the bottom of a cylindrical dish (diameter: 2 cm) containing water (≈3 mm high). In our experiments, the dish was small enough that the mixture reached the border within a time smaller than the time at which cells formed; thus, λ did not grow due to the expansion of the drop, as we had observed in larger dishes.

The mixture in the dish was illuminated with white light from above, while the formation of cells was monitored (by determining the light absorbtion of S) from below by a light microscope connected to an image acquisition equipment. The mean size of the cells (wavelenghth λ) was determined by two-dimensional Fourier transforms of the images, averaging (at fixed T_0 and r_ρ) over 50 independent experiments. In order to

keep the time between experimental initiation and evaluation short and to have, at the same time, largest optical contrast, we determined λ when all minima of the absorbed light were within 5% of the intensity measured with a void dish. The time—after initiation of the experiment—at which this condition was fulfilled was what we defined as emergence or growth time T_{em}.

The left part of Fig. 1 shows typical images with a large (Fig. 1a) and a small (Fig. 1b) λ. Fig. 2 shows T_{em} and λ, both vs. T_0, for different values of r_ρ. The fitted straight lines in Fig. 2 correspond to the scaling laws

$$T_{\mathrm{em}} \sim T_0^{-\gamma_T} \tag{1}$$

$$\lambda \sim T_0^{-\gamma_\lambda} \tag{2}$$

Note that the values of T_{em} and λ for a given value of T_0 (we call these values $\widetilde{T}_{\mathrm{em}}$ and $\tilde{\lambda}$ for $T_0 = 2.5\%$) depend strongly on r_ρ. In contrast, the exponents γ_T and γ_λ (slopes in Fig. 2) are quite robust to changes in r_ρ, as seen by the nearly parallel displacement of the straight lines in Fig. 2. The values of γ_T, γ_λ, $\widetilde{T}_{\mathrm{em}}$ and $\tilde{\lambda}$ for $r_\rho = 1$ are given in Table 1 under the heading "exp".

Another set of experiments was performed using nondairy coffee-creamer. We did quantitative evaluations with the german brand "Cafita", and we found that brands available in other countries (e.g. "Coffee-Mate") behave similarly. Such whiteners contain surfactants which take up the role of S, as well as sugar, which plays the role of T. The whitener powder was mixed with water, stirred and injected as in the experiments described above. The measured T_{em} and λ (averaged over 50 independent experiments) vs. T_0 is shown in Fig. 5 (symbols denoted by "$\mathrm{exp_w}$"). Because the components of the whitener are fixed and quantitatively unknown to us, we could not change T_0 and S_0 independently. However, r_ρ is constant for the points shown in Fig. 5, as they were obtained using differently diluted samples of the same powder. The exponents and the values for $T_0 = 2.5\%$, as obtained from these experiments and plotted in Fig. 5, are given in Table 1 (heading $\mathrm{exp_w}$).

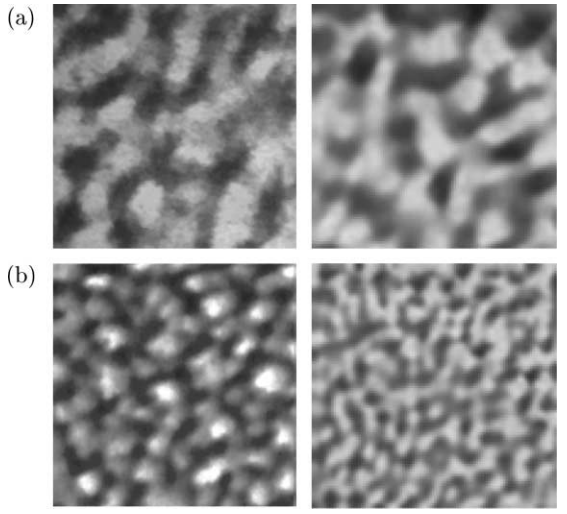

Fig. 1. Left: light absorption measurements. Right: PDE simulations initialized by injection.

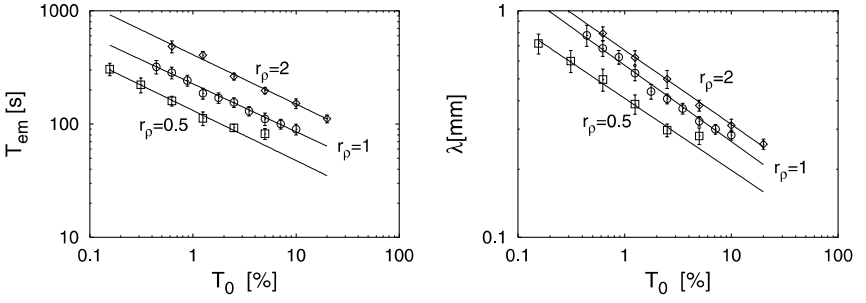

Fig. 2. Experimental results.

Table 1
Exponents (γ_T, γ_λ) and values of T_{em} and λ at $T_0 = 2.5\%$ ($\widetilde{T}_{\mathrm{em}}$, $\tilde{\lambda}$) corresponding to Fig. 5

	exp	$\mathrm{sim_i}$	$\mathrm{sim_l}$	$\mathrm{sim_h}$	theor	$\mathrm{exp_w}$
γ_T	0.42 ± 0.03	0.43 ± 0.02	0.56 ± 0.02	0.67 ± 0.02	2/3	0.51 ± 0.03
γ_λ	0.34 ± 0.02	0.33 ± 0.02	0.30 ± 0.01	0.33 ± 0.01	1/3	0.38 ± 0.02
$\widetilde{T}_{\mathrm{em}}$ (s)	153 ± 31	224 ± 18	225 ± 17	136 ± 11	–	285 ± 43
$\tilde{\lambda}$ (mm)	0.42 ± 0.03	0.35 ± 0.02	0.18 ± 0.01	0.15 ± 0.01	–	0.49 ± 0.04

$\widetilde{T}_{\mathrm{em}}$ and $\tilde{\lambda}$ were determined from the fitted scaling laws.

3. Analytical estimates

A perturbation A grows as

$$A \sim \exp(\Lambda t) \tag{3}$$

where the growth rate Λ is given by

$$\Lambda \sim \overline{T}_z^{1/2} g(R_\rho) \tag{4}$$

[19]. $R_\rho = a_T \overline{T}_z/(\alpha_S \overline{S}_z)$, $\alpha_T = (\rho_T - \rho_0)/\rho_0$, $\alpha_S = (\rho_S - \rho_0)/\rho_0$. $\overline{T}_z$ and $\overline{S}_z$ are the vertically averaged gradients $\partial T/\partial z$ and $\partial S/\partial z$, respectively.

We consider times small enough to approximate $T \approx T_0$ at $z = 0$. Thus, $\overline{T}_z = T_0/h(t)$ and $\overline{S}_z = S_0/h(t)$; where $h(t)$ is the height of the expanded drop in our case. $h(t)$ grows vertically by diffusion as $h(t) \sim t^{1/2}$, while the area of the layer remains unchanged. These approximations yield $\Lambda \sim T_0 t^{-1/2} g(R_\rho)$ and $R_\rho \sim r_\rho = T_0/S_0$.

In a more formal analytical calculation [12], one obtains $T_z \sim T_0 t^{-1/2} \exp(-z^2/(4D_T t))$ and $R_\rho = (T_0/S_0) \exp(0.5 z^2 t^{-1}(D_S^{-1} - D_T^{-1}))$. Using these relationships, the results for Λ and r_ρ obtained in the preceeding paragraph remain unchanged if one considers the maximum of T_z (corresponding to the dominant value of the growth rate Λ) instead of $\overline{T}_z$.

Under consideration of the time dependence of Λ, Eq. (3) must be replaced by

$$A \sim \exp\left(\int_0^t \Lambda(t')\,\mathrm{d}t' \right) \tag{5}$$

For each set of measurements aimed to determine the scaling laws in our experiments, we hold $r_\rho = T_0/S_0 = \text{const}$; thus, $R_\rho \approx \text{const}$. Therefore,

$$\int_0^t \Lambda(t')\,\mathrm{d}t' \sim \int_0^t \left(T_0 t'^{-1/2}\right)^{1/2} \mathrm{d}t' \sim T_0^{1/2} t^{3/4} \tag{6}$$

In our experimental evaluations (at $t = T_{\mathrm{em}}$), we required that a pertubation A has an approximately fixed value, namely that at which minima are within 5% of the value for a void dish. Therefore, Eqs. (5) and (6) yield $T_0^{1/2} t^{3/4} = \text{const}$, or

$$T_{\mathrm{em}} \sim T_0^{-2/3} \tag{7}$$

For the wavelength, it has been shown [20] that

$$\lambda \sim \overline{T}_z^{-1/4} \tag{8}$$

Thus, $\lambda \sim \left(T_0 t^{-1/2}\right)^{-1/4}$. Setting $t = T_{\mathrm{em}}$ and considering Eq. (7) we obtain

$$\lambda \sim T_0^{-1/3} \tag{9}$$

Eqs. (7) and (9) predict $\gamma_T = \frac{2}{3}$ and $\gamma_\lambda = \frac{1}{3}$. These values appear in Table 1 under the heading "theor".

Estimates for the deviations from $\gamma_T = \frac{2}{3}$ and $\gamma_\lambda = \frac{1}{2}$ by virtue of the exponential functions involved in T_z and R_ρ (see above) are extremely difficult in our case. In fact, for such estimates, we could not assume, as we have done, a constant R_ρ; dropping this assumption would imply a considerable numerical effort because the function $g(R_\rho)$ in Eq. (4) is difficult to handle and to comprehend [19]. We therefore preferred to test our analytical approximations by comparing them with PDE simulations, as will be described in the next sections.

4. Numerical simulations

We consider the PDEs for an incompressible, hydrodynamic system with two dissolved substances S and T:

$$\partial_t \vec{v} + (\vec{v}\vec{\nabla})\vec{v} = \frac{\rho}{\rho_0}\vec{g} - \frac{1}{\rho_0}\vec{\nabla}p + \nu\Delta\vec{v} \tag{10}$$

$$\vec{\nabla}\vec{v} = 0 \tag{11}$$

$$\partial_t S + (\vec{v}\vec{\nabla})S = D_S \Delta S \tag{12}$$

$$\partial_t T + (\vec{v}\vec{\nabla})T = D_T \Delta T \tag{13}$$

$$\frac{\rho}{\rho_0} = 1 + \alpha_T T + \alpha_S S \tag{14}$$

For initialization of the unstable behaviour, we set $\vec{v}$ at $t = 0$ equal to noise vectors $\vec{\epsilon}$; the directions and magnitudes of $\vec{\epsilon}$ were chosen randomly and homogeneously distributed with the restriction $|\vec{\epsilon}| \in [0, 10^{-2}]$ mm/s. In order to prevent border effects, we used cyclic boundary conditions in the horizontal directions; at the bottom and at the top, we imposed no-slip boundary conditions for $\vec{v}$ and no-flux boundary conditions for S and T. The equations were integrated using the finite volume method on a colocated grid with an implicit three time level scheme, central difference scheme and the SIMPLE algorithm for pressure correction [21]. The time step was set to $\Delta t = 0.1$ s. When the injection process was not considered, we set the uniform grid size to 10^{-2} mm and the simulated domain to $1 \times 1 \times 1$ mm^3. When considering the injection process, we set the grid size to 4×10^{-2} mm and the domain size to $10 \times 10 \times 3$ mm^3. We determined the numerical stability by finding out that the same results were obtained if we used half the time step as well as half the grid sizes in simulations with the highest and lowest values of T_0 in all considered cases.

For the simulation of the injection with a pipette, we considered in the simulations a cylinder (diameter: 0.8 mm) centered with the domain and extending upwards. Its base was 0.5 mm above the bottom. Within this cylinder, $S_0 = \text{const}$, $T_0 = \text{const}$ and $\vec{v} = (0,\ 0,\ -1.6)$ mm/s for $t < 20$ s. The wall of the pipette was considered by setting all variables to zero within a region around the cylinder having a thickness of 0.16 mm. At $t = 20$ s, the regions occupied by the pipette and its wall were replaced by a region with $S = T = 0$, having no

boundaries and thus interacting thereafter with the rest of the medium.

v was set to 1.1×10^{-6} m^2/s. Capillary measurements showed no significant changes of this value within the considered ranges of T_0 and S_0, so that v was hold constant throughout the work. The diffusion coefficient of glycerine is $D_T = 10^{-10}$ m^2/s. X-ray small-angle scattering measurements, as well as kinetic measurements of finger-thickening [16], allowed to estimate $D_S = 3 \times 10^{-12}$ m^2/s.

Fig. 3 shows the time evolution of S-fingers in a two-dimensional simulation using Eqs. (10)–(14). We started these simulations by assuming $S = T$ increasing linearly downwards—within the lower layer—from 0 to 5 vol.% (Fig. 3a). Fig. 3b illustrates results at $t = T_{em}$. In contrast to the S-fingers, the distribution of T is almost constant in the horizontal direction owing to $D_T \gg D_S$.

Since we wanted to know how strongly the initial configuration influences the results, we performed three-dimensional simulations using three different initializations: (I) homogeneous distribution at $t = 0$ in the lower layer ($T_0 = \text{const}$, $S_0 = \text{const}$ for $z < 0.16$ mm, $T_0 = S_0$ elsewhere); (II) linear distribution at $t = 0$ in the lower layer (S and T increase linearly downwards from 0 to S_0 and T_0 for $z < 0.32$ mm; $T = S = 0$ elsewhere); (III) simulation of the injection of the mixture through a cylinder as described above.

Fig. 4 illustrates simulations considering the injection process. The horizontal, upper border of the black region in Fig. 4a corresponds to the lower border of the injection pipette. The two pictures on the right part of Fig. 1 show enlarged sections of configurations such as the one in Fig. 4c.

Fig. 5 shows T_{em} and λ vs. T_0, as obtained in three-dimensional simulations (with $r_\rho = 1$) using the three initializations (I) through (III) given above. Since the signal to noise ratio is much higher than in experiments, each simulated point in Fig. 5 corresponds to only one pattern, in contrast to the 50 images evaluated in experiments. The values of γ_T, γ_λ, $\tilde{T}_{em}$ and $\tilde{\lambda}$ are given in Table 1 under the headings "sim$_h$", "sim$_l$" and "sim$_i$" for initializations with an homogeneous distribution, with a linear distribution and with the injection process, respectively. For better visualization, errors of the points in Fig. 5 are not shown; note that the inaccuracies given in Table 1 result both from these errors and from the deviations of the points in Fig. 5 around fitted straight lines.

Fig. 5 and Table 1 were obtained assuming $r_\rho = 1$. Simulations with $r_\rho = 0.5$, initialized with a linear distribution of S and T, yield $\gamma_T = 0.56 \pm 0.01$, $\gamma_\lambda = 0.29 \pm 0.01$, $\tilde{T}_{em} = 71 \pm 11$ s and $\tilde{\lambda} = 0.16 \pm 0.01$ mm, (experimental values for $r_\rho = 0.5$, corresponding to Fig. 2, are: $\gamma_T = 0.44 \pm 0.02$, $\gamma_\lambda = 0.32 \pm 0.02$, $\tilde{T}_{em} = 90 \pm 11$ s and $\tilde{\lambda} = 0.29 \pm 0.02$ mm). Simulations with $r_\rho = 2$, also

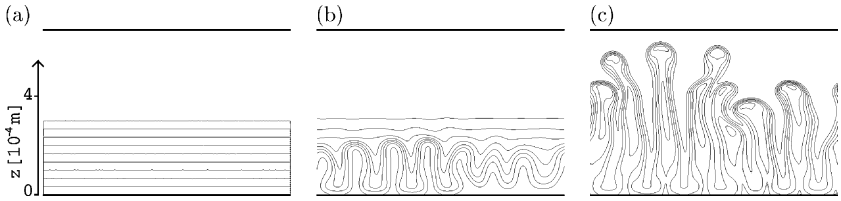

Fig. 3. Lines with equal S obtained from two-dimensional PDE simulations. The ordinates and the lengths of the abcissa (1 mm) are the same for (a)–(c). (a) $t = 0$ s; (b) $t = 200$ s; (c) $t = 280$ s.

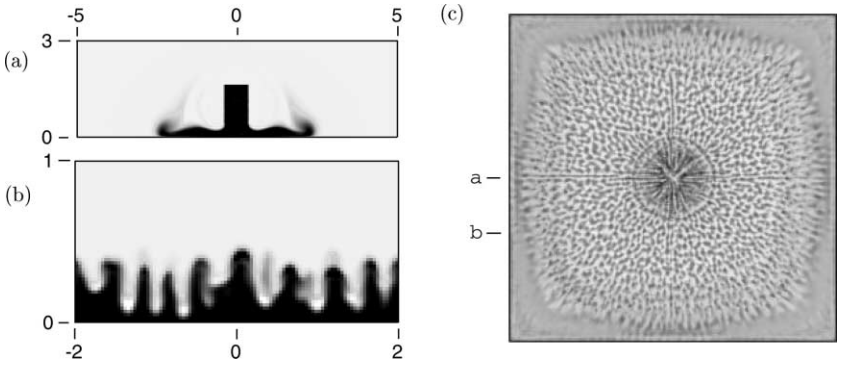

Fig. 4. Three-dimensional PDE simulations initiated by injection. S is shown by grey levels, $T_0 = 5\%$, $r_\rho = 1$. (a,b) Side views of sections in the directions indicated in the picture on the right. The numbers in (a) and (b) indicate the distance in millimeter horizontally from the center or vertically from the bottom. (a) $t = 15$ s, (b) $t = 240$ s. (c) View from above $t = 240$ s, 10×10 mm^2.

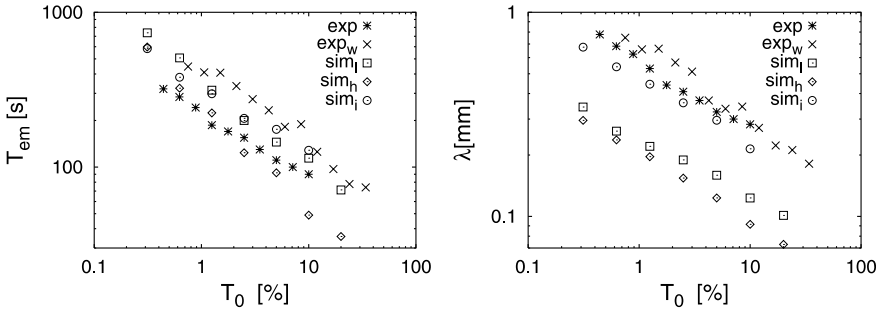

Fig. 5. Results from experiments and three-dimensional PDE simulations. $r_\rho = 1$. exp: Experiments with the surfactant–glycerine mixture. exp_w: experiments with the whitener. sim_i: simulations initiated with injection. sim_h: simulations initiated with homogeneous distributions. sim_l: simulations initiated with linear distributions.

initialized with a linear distribution, yield $\gamma_T = 0.54 \pm 0.01$, $\gamma_\lambda = 0.29 \pm 0.01$, $\widetilde{T}_{em} = 550 \pm 42$ s and $\tilde{\lambda} = 0.20 \pm 0.01$ mm (experimental values for $r_\rho = 2$, corresponding to Fig. 2, are: $\gamma_T = 0.44 \pm 0.02$, $\gamma_\lambda = 0.33 \pm 0.02$, $\widetilde{T}_{em} = 281 \pm 23$ s and $\tilde{\lambda} = 0.50 \pm 0.04$ mm).

5. Conclusions

At a first glance, the integration of PDEs yields cells that are comparable to experimental observations (Fig. 1). Varying T_0 within a factor 25, the evaluation of experiments for different r_ρ yields power laws for T_{em} and λ vs. T_0 (Fig. 2). The large number of evaluated experimental images permitted to reduce the error, so as to increase the confidence for the linearity of the log–log plots over the whole investigated range.

In analytical or numerical calculations, the value of the exponent γ_λ ($\approx$0.3) is extremely robust to varying model assumptions. Moreover, this exponent agrees well with the experimental values. In contrast, the value of the exponent γ_T is more sensitive to model assumptions; in fact, only the simulations starting with injection yield a value comparable to experiments with the well-defined surfactant–glycerine mixture ($\approx$0.4), while the other calculated values are in the range 0.6–0.7. The model with injection also leads values for $\tilde{\lambda}$ that are closer to experiments than the other models. On the other hand, our analytical estimates $\gamma_T = \frac{2}{3}$ and $\gamma_\lambda = \frac{1}{3}$ (as derived in Section 3) agree well with the values obtained from PDE simulations with linear or homogeneous initial distributions (under the headings 'sim_l' and 'sim_h' in Table 1).

As for the experiments involving the whitener, it is remarkable that γ_λ, γ_T and $\tilde{\lambda}$ are not far from the other experiments and from calculations with injection. However, $\widetilde{T}_{em}$ differs considerably for the whitener, surely owing to the different physico-chemical properties of the material (which are unknown to us) and to the fact that the whitener contains a mixture of surfactants (mono- and diglycerides). We must keep in mind that the lack of precise chemical definition and the impossibility of controlling the components makes the whitener inappropriate for quantitative research; however, we found the system with the whitener—being easy to implement—most useful for phenomenological and educational tasks.

Adopting a generous attitude towards the discrepancies discussed above, one is astonished (when regarding Fig. 5) about the qualitative (and partially quantitative) convergence of results from different models and different experimental setups. The fact that the general and highly approximate analytical estimations are not too far from sophisticated PDE simulations, as well as from experiments (including those with unknown mixtures of surfactants) suggests a general validity of the power laws reported here. This should be kept in mind in future investigations with related systems.

Acknowledgements

This work was supported by the Deutsche Forschungsgemeinschaft (Grants Ma 629/5).

References

[1] H.E. Huppert, J.S. Turner, Double-diffusive convection, J. Fluid Mech. 106 (1981) 299–329.
[2] C.F. Chen, D.H. Johnson, Double-diffusive convection: a report on an engineering foundation conference, J. Fluid Mech. 138 (1984) 405–416.
[3] J.S. Turner, Multicomponent convection, Ann. Rev. Fluid Mech. 17 (1985) 11–44.
[4] A.J. Williams, Salt fingers observed in mediterranean outflow, Science 185 (4155) (1974) 941–943.
[5] T.G.L. Shirtcliffe, J.S. Turner, Observations of cell structure of salt fingers, J. Fluid Mech. 41 (1970) 707–719.
[6] S.R. Coriell, M.R. Cordes, W.J. Boettinger, R.F. Sekerka, Convective and interfacial instabilities during unidirec-

tional solidification of a binary alloy, J. Cryst. Growth 49 (1) (1980) 13–28.
[7] A.R. McBirney, R.M. Noyes, Crystallisation and layering of the Skaergaard intrusion, J. Petrol. 20 (3) (1979) 487–554.
[8] J. Schmitt, R. Rosner, Doubly diffusive magnetic buoyancy instability in the solar interior, Astrophys. J. 265 (1983) 901–924.
[9] E.A. Spiegel, Convection in stars. 2. Special effects, Ann. Rev. Astronom. Astrophys. 10 (1972) 261–304.
[10] H.B. Fisher, The dilution of an undersea sewage cloud by salt fingers, Water Res. 5 (1971) 909–915.
[11] H.E. Huppert, P.C. Manins, Limiting conditions for salt-fingering at an interface, Deep-Sea Res. 20 (4) (1973) 315–323.
[12] T.G.L. Shirtcliffe, Transport and profile measurements of diffusive interface in double-diffusive convection with similar diffusivities, J. Fluid Mech. 57 (1973) 27–43.
[13] J.R. Taylor, G. Veronis, Experiments on double-diffusive sugar-salt fingers at high stability ratio, J. Fluid Mech. 321 (1996) 315–333.
[14] P.F. Linden, Structure of salt fingers, Deep-Sea Res. 20 (4) (1973) 325–340.
[15] J.S. Turner, Salt fingers across a density interface, Deep-Sea Res. 14 (5) (1967) 599–611.
[16] K. Kötter, M. Markus, Double-diffusive fingering instability of a surfactant–glycerine–water drop in water, Europhys. Lett. 55 (6) (2001) 807–813.
[17] M. Markus, K. Kötter, Of icebergs and coffee creamers, Educ. Chem. July (2001) 108.
[18] E. Kunze, Limits on growing finite length salt fingers—A Richardson-number constraint, J. Marine Res. 45 (3) (1987) 533–556.
[19] R.W. Schmitt, The characteristics of salt fingers in a variety of fluid systems, including stellar interiors, liquid metals, oceans and magmas, Phys. Fluids 26 (9) (1983) 2373–2377.
[20] M.E. Stern, The salt-fountain and thermohaline convection, Tellus 12 (22) (1960) 172–175.
[21] J.H. Ferzinger, M. Peric, Computational Methods for Fluid Systems, Springer, New York, 1997.